Archives of Toxicology (2018) 92:3291–3305
https://doi.org/10.1007/s00204-018-2306-9

NANOTOXICOLOGY

Carbon nanotubes and crystalline silica induce matrix remodeling and contraction by stimulating myofibroblast transformation in a three-dimensional culture of human pulmonary fibroblasts: role of dimension and rigidity

Bridget Hindman[1] · **Qiang Ma**[1]

Received: 4 August 2018 / Accepted: 13 September 2018 / Published online: 18 September 2018

Abstract
Pulmonary fibrosis is a poorly understood pathologic condition. Carbon nanotubes (CNTs) are nanomaterials with potentials for broad applications. CNTs can induce pulmonary fibrosis in animals, a cause for concern for exposed workers and consumers. Given the large number of CNTs available on the market and the seemingly infinite number of ways these particles can be modified in ways that may affect toxicity, in vitro models that can be used to quickly and effectively investigate the relative fibrogenicity of CNTs are much needed. Here we analyzed the fibrogenic potentials of six CNTs of varying physical properties and crystalline silica using two- and three-dimensional (2D and 3D, respectively) in vitro models. WI38-VA13 human pulmonary fibroblasts were treated with CNTs or silica, with TGF-β1, a known inducer of fibroblast differentiation, as positive control. The cells were examined for fibrotic matrix alterations, including myofibroblast transformation, matrix remodeling, and matrix contraction. While all tested CNTs induced myofibroblast differentiation in 2D and 3D cultures, the 3D culture allowed the examination of myofibroblast clustering, collagen deposition and rearrangement, cell division, and matrix contraction in response to fibrogenic exposures, processes critical for fibrosis in vivo. At 1 μg/ml, MWCNTs elicit higher induction of myofibroblast differentiation and matrix remodeling than SWCNTs. Among MWCNTs, those with the highest and lowest aspect ratios produced the largest effects, which were comparable to those by TGF-β1 and higher than those by silica. Thus, the 3D collagen-based model enables the study of matrix fibrotic processes induced by CNTs and silica particles directly and effectively.

Keywords CNT · Silica · Fibrosis · 3D culture · Myofibroblast · Matrix remodeling

Introduction

Pulmonary fibrosis is a devastating pathologic condition caused by a buildup of scar tissue in the lungs, leading to destruction of lung architecture and respiratory failure. While pulmonary fibrosis often represents the common end-stage development in many respiratory disease conditions, exposures to certain physical, chemical, and biological factors result in induced lung fibrosis. Of particular importance to occupational and environmental safety and health are the emerging and new fibrogenic materials that workers may encounter during the manufacturing process, and consumers may be exposed to when using commercial products containing these materials (Donaldson et al. 2006; Dong and Ma 2015).

Carbon nanotubes (CNTs) are nanomaterials made of one-atom-thick graphene sheets in the form of single-walled (SWCNT) or multi-walled (MWCNT) cylindrical nanostructures. Owing to their excellent mechanical strength, thermal conductivity, and electrical and optical properties, CNTs have been developed with a wide range of applications for both industrial and commercial uses. As such, there have been largely increased annual productions of CNTs and

✉ Qiang Ma
qam1@cdc.gov

[1] Receptor Biology Laboratory, Toxicology and Molecular Biology Branch, Health Effects Laboratory Division, National Institute for Occupational Safety and Health, Centers for Disease Control and Prevention, Morgantown, WV, USA

CNT-containing products worldwide in the recent decade (NSF 2011). However, their nanoscale size, fiber-like shape, and high respirability and biopersistence are often associated with fibrogenic and tumorigenic activities observed in toxic fibers such as asbestos. Indeed, many forms of CNTs have been shown to cause pulmonary fibrosis in laboratory animals (Dong and Ma 2016c, 2017a, b; Dong et al. 2015; Mitchell et al. 2007; Porter et al. 2010).

A majority of the studies investigating the toxicity of CNTs focus on the potential of these nanomaterials to induce fibrosis in animal models (Dong and Ma 2015). However, animal testing is expensive and time consuming. Given the vast number of CNTs available on the market and the seemingly infinite number of ways these particles can be modified that may affect toxicity, in vitro models that can be used to quickly and efficiently investigate the relative toxicity of different CNTs would be an invaluable asset. Such in vitro systems would need to reflect the in vivo pulmonary fibrotic processes induced by CNTs with regard to key properties and dynamics of fibrotic development (Duffield et al. 2013). This has been a very challenging task to investigators hoping to characterize the fibrogenic potentials of CNTs and CNT-containing materials.

CNT-induced fibrotic lesions bear certain similarity to those observed in pneumoconiosis and idiopathic pulmonary fibrosis (IPF), diseases that are frequently progressive and incurable. In these scenarios, the hallmark of fibrosis is the excessive deposition of collagen fibers in the extracellular matrix (ECM) that leads to alveolar and airway remodeling, matrix contraction, and progressive scarring of the lungs, and eventual loss of lung compliance (Dong and Ma 2016b; Duffield et al. 2013). At the cellular level, the fibrotic development depends on the activation and differentiation of fibroblasts to myofibroblasts. Myofibroblasts are characterized by their high capacity of collagen production and their de novo synthesis of α-smooth muscle actin (α-SMA) that incorporates into stress fibers for enhanced cell contraction. These cells are responsible for producing a major portion of collagen and other matrix proteins in fibrotic foci and for mediating the contraction of fibrotic tissues (Van De Water et al. 2013).

Formation of fibrotic matrix involves complex and dynamic interactions of fibroblasts and myofibroblasts with their surrounding environment. Upon activation, lung fibroblasts migrate to the site of injury where they proliferate and differentiate into myofibroblasts. These myofibroblasts actively remodel the matrix by secreting copious amounts of collagen and other fibrotic matrix proteins, rearranging collagen fibers, and contracting the matrix, which increases the stiffness of the matrix leading to scar formation. The matrix plays a prominent role in the continued activation of myofibroblasts and the progression of fibrosis (Blaauboer et al. 2014; Liu et al. 2010; Marinkovic et al. 2012). The matrix directly contributes to the signal transduction that regulates various aspects of fibrotic responses, such as activation of the latent form of tissue transforming growth factor (TGF)-β1. Increased stiffness also directly stimulates fibroblasts to proliferate and to migrate toward foreign body deposits through a process called durotaxis. In this manner, fibroblasts and their matrix form a positive feed-forward loop to foster and sustain fibrotic progression.

In this study, human pulmonary fibroblasts were exposed to CNTs of varying physical properties and crystalline silica to evaluate their fibrogenic potentials by using in vitro systems that mimic in vivo fibrotic responses. The fibrogenic potentials of these particles were first examined for their ability to induce myofibroblast activation in a two- or three-dimensional (2D and 3D, respectively) model. Importantly, the 3D collagen gel made it possible to examine directly the morphology, process formation, and behaviors of myofibroblasts, as well as their interactions with particulates and other cells, in three dimensions. Moreover, the 3D culture enabled the visualization and quantification of myofibroblast clustering, collagen deposition and rearrangement, cell division, and matrix contraction in response to CNT exposures. At an equal concentration, MWCNTs elicited higher induction of myofibroblast differentiation and matrix remodeling than SWCNTs, and among the MWCNTs, those with highest and lowest aspect ratios produced the largest effects, which were comparable to those by TGF-β1 and higher than those by silica. These findings demonstrate that 3D collagen-based model can be used to study matrix fibrotic processes induced by CNTs and silica directly and effectively.

Materials and methods

Cell culture

The human pulmonary fibroblast cell line WI38-VA13 was acquired from ATCC (Manassas, VA, USA). Cells were maintained in minimum essential medium-α supplemented with 10% fetal calf serum (FCS), and 1× antibiotic–antimycotic (ThermoFisher Scientific, Waltham, MA, USA). Cultures were maintained at 37 °C in a humidified 5% CO_2 incubator.

Sources and characterization of CNTs and silica

CNTs of various dimensions were acquired to examine their fibrotic potential. CNTs were given labels based on their physical dimensions and rigidity. MWCNTs with relative physical dimensions of long and slender (M-LS), intermediate (M-IM), and short and slender (M-SS), were purchased from Sigma Aldrich (St. Louis, MO, USA). XNRI MWNT-7 was originally from Mitsui & Company (Tokyo, Japan) and

were considered short and rigid (M-SR) based on previous characterizations (Dong et al. 2015; Duke et al. 2017; Porter et al. 2010). SWCNTs of both long (S-L) and short (S-S) lengths were also purchased from Sigma Aldrich. Crystalline silica (Min-U-Sil 5) was from US Silica (Berkeley Springs, WV, USA).

Properties of the particulate materials used are summarized as the following. Briefly, M-LS have an average diameter of 12 nm, an average length of 10 µm, and a specific surface area of 200 m^2/g. M-IM have an average diameter of 10 nm, an average length of 3–6 µm, and a specific surface area of 280–350 m^2/g. M-SS have an average diameter of 9.5 nm, an average length of 1 µm, and a specific surface area of 300 m^2/g. M-SR have an average diameter of 49 nm, an average length of 3.68 µm (Porter et al. 2010), and a specific surface area of 22 m^2/g (Birch et al. 2013). For SWCNT samples used, S-L have a diameter of 0.7–1.1 nm, a length of 0.3–2.3 µm, and a specific surface area of 700 m^2/g (Teran 2016), whereas S-S have a diameter of 1–2 nm, a length of 0.5–2 mm, and a specific surface area of 480 m^2/g. The aspect ratios were substantially higher for the SWCNTs, as well as M-LS, followed by M-IM and M-SS, and lastly by M-SR. The MIN-U-SIL 5 silica has 97% of the particles within 5 µm with a median diameter of 1.6 µm. The specific density of the particles is 2.65 and their content for silicon dioxide (SiO_2) is 99.2% and content for iron oxide (Fe_2O_3) 0.035%.

All particulate inducers were dispersed in culture media with 1% FCS at a stock concentration of 2 mg/mL by vortex (three times, 2 min each) and sonication (three times, 30 s each; 40% output; Ultrasonic Processor, GE 70T, Fisher Scientific, Pittsburgh, PA). Stock solutions were further diluted with the culture media and sonicated immediately before use. Vehicle control (VC) samples were treated with an equal amount of the dispersion medium (media with 1% FCS) to establish a baseline response and validate that there was no effect on the cells from the dispersion medium.

Suspended CNTs were imaged using transmission electron microscopy (TEM). Stock samples as prepared above were further diluted in double distilled H_2O to 1:300 for most of the samples. M-IM and M-SS were further diluted to 1:600 to obtain images of single fibers. One drop of the diluted samples was placed onto a formvar-coated 200 mesh copper grid and allowed to dry overnight. The samples were imaged in a JEOL 1400 TEM (Tokyo, Japan) at 80 kV.

Flow cytometry and immunofluorescence staining

Fibroblasts were treated with vehicle, various particulate inducers (1 µg/mL), or TGF-β1 (2 ng/mL; Sigma Aldrich), a positive control for myofibroblast differentiation, for 24 h before being trypsinized and stained in preparation for flow cytometry analysis of α-SMA expression. Briefly, after trypsinization, cells were centrifuged at 300×*g* for 10 min, fixed in cold 0.01% formaldehyde and permeabilized in 0.5% Tween 20 (v/v in phosphate buffered saline or PBS). Cells were then washed three times with cold PBS, followed by centrifugation at 300×*g* for 5 min, before being incubated in a 1:500 dilution of a monoclonal α-SMA antibody (Sigma Aldrich) in permeabilization buffer. After thoroughly washing cells in cold PBS, cells were incubated with Alexa 488 goat α-mouse secondary antibody (A11001, ThermoFisher) in permeabilization buffer. Cells were then washed in cold PBS, resuspended in 1% formaldehyde, and stored for less than 2 h before analysis using a LSRII Flow Cytometer (BD Sciences, San Jose, CA, USA). Staining controls were performed using IgG that matched the primary antibody. For each sample, 10×10^4 events were acquired and the same instrument settings were used for each experiment. Initial gating and analysis were performed using the FACSDiva software (Version 6, San Jose, CA, USA). Dot plots were generated using Flowing Software (Version 2.5.1, Perttu Terho, Turku Center for Biotechnology, Turku, Finland).

Immunofluorescence staining for 2D and 3D cultures was performed using standard procedures. After 24 h incubation with fibrotic inducers, samples were fixed in 4% formaldehyde, permeabilized in 0.5% Triton X-100, and stained overnight at 4 °C with TRITC Phalloidin (Sigma Aldrich) and monoclonal anti-α-SMA antibody (Sigma Aldrich). Secondary antibody (Alexa 488 goat anti-mouse) was used at a final dilution of 1:1000 and samples were mounted in Vectashield mounting media with DAPI (Vector Labs, Burlingame, CA, USA). Samples were imaged using a Zeiss 780 confocal microscope with a Plan-Apochromat 63×/1.40 Oil DIC M27 objective. The full depth of the cell monolayer was imaged at a *z*-step of 0.5 µm. The average cellular α-SMA content was analyzed using Image J software (Version 1.5.1 g, NIH, Bethesda, MD, USA). For each treatment, 50 cells were evaluated for α-SMA quantification.

For 3D samples, staining was performed on small sections cut from collagen constructs generated as described and images were obtained using a Zeiss 780 confocal microscope with an EC Plan-Neofluar 40×/1.30 Oil DIC M27 objective and 100 µm sample images were taken at 1 µm *z*-step intervals. The cellular α-SMA content was analyzed and surface projections were generated using IMARIS software (Version 8.4.1, Bitplane, Zurich, Switzerland).

Histopathology

Collagen solutions containing cells and particles were prepared. After the cells were allowed to remodel the collagen matrix for 48 h, the samples were fixed in 4% formalin, embedded in paraffin blocks, and processed for Masson's trichrome staining or immunohistochemistry staining as described previously (Dong and Ma 2017b). Images

obtained at 10× magnification (UPlanFLN 10×/0.30 Ph1) were used for collagen staining, cell cluster number, and cell cluster area analysis. Images of the same area obtained at 100× (UPlanSApo 100×/1.40 oil) magnification were used for collagen fiber orientation analysis. The relative amount of collagen staining was analyzed in ImageJ. As an analogous measure to fibrotic foci measurements in biopsy samples from lung samples, we evaluated the number of "cell clusters". For this purpose, a "cell cluster" was defined as a group of three or more cells that share a surrounding reorganized collagen matrix, as indicated by visible changes in the collagen staining pattern. The total number of cell clusters per square millimeter was calculated from images across three separate samples. The total cell cluster area was calculated using ImageJ. A region of interest was drawn around each cell cluster, including the surrounding altered matrix, and the area measured. The sum was then used to calculate the cell cluster area as a percentage of the total imaged area. For IHC staining analysis, 20× and 100× magnification images were obtained and the percentage of cells expressing Ki67 determined using ImageJ.

Gel contraction assay and collagen fiber orientation analysis

Gel contraction assays were carried out as described previously (Lygoe et al. 2004). Briefly, fibroblasts were combined with 1 mg/mL Type I rat tail collagen (Corning, Corning, NY, USA) at a density of 1×10^5 cells/mL and the collagen solution was neutralized with 0.1 N sodium hydroxide. For treated samples, particulate inducers (1 µg/mL) or TGF-β1 (2 ng/mL) were added directly to the collagen/cell solution and briefly vortexed to ensure an even distribution of the particulates throughout the samples as described previously (MacDonald et al. 2005). A volume of 0.5 mL of the solution was added to a 24-well plate. After the collagen was allowed to polymerize in a humidified incubator for 30 min, the gels were detached from the plate by gently running a 200 µL pipet tip around the circumference of the gel. Plates were imaged at 0, 24, and 48 h thereafter and the percent contraction was calculated by measuring the change in gel diameter. Samples were poured in triplicate for each treatment and the experiment was replicated three times.

To analyze the physical changes made to the collagen matrix after cells are treated with CNTs, we used the OrientationJ plug-in for ImageJ to calculate the coherency coefficient of the collagen fibers in treated samples. OrientationJ measures the orientation angle of fibers in each image and calculates the coherency coefficient as a value between 0 and 1. A coherency coefficient of 0 indicates no preferential orientation angle in the fibers, as seen in essentially randomly oriented samples and with no significant alignment along any direction. A coherency coefficient of 1 indicates a strong preferential orientation angle (Puspoki et al. 2016; Rezakhaniha et al. 2012). In other words, a group of fibers with a coherency coefficient of 1 are strongly aligned in a single direction. For each image, the alignment of the collagen in the area immediately surrounding the cells, but excluding the cells, was measured. Five measurements were taken for each image, with 3 images taken per sample across 3 samples for a total of 45 measurements.

Statistical analysis

Statistical analysis was performed using GraphPad Prism software (Version 7.02, GraphPad Software Inc., La Jolla, CA, USA). All experiments were performed in triplicate and experiments were repeated three times. Data are presented as mean ± SD. Statistical significance was determined using one-way ANOVA followed by a Tukey post-test for between sample comparisons. *, $p < 0.05$; **, $p < 0.01$; and ***, $p < 0.001$.

Results

Characterization of particulate inducers

CNTs of various physical dimensions and crystalline silica particles were acquired in order to measure and compare their fibrogenic potentials in an in vitro model of tissue fibrosis. Their physical dimensions and characteristics were provided under "Materials and methods". The dimensions and appearances in solution of the CNTs were assessed using TEM (Fig. 1). M-LS had a relatively long and slender appearance, with some single fiber tangles or fiber aggregates observed. M-IM appeared to have more variability in length. M-SS were likely to form aggregates; in some cases, fibers were wrapped around each other, forming a rope-like structure. M-SR were visibly thicker and thus more rigid than the other MWCNTs. Additionally, few individual fiber tangles or fiber aggregates were observed for M-SR. Both S-L and S-S formed rope-like structures as described for M-SS fibers, even at higher dilutions and with increased sonication.

CNTs and crystalline silica induced robust α-SMA expression in fibroblasts

A hallmark of fibrogenic responses is the transformation of fibroblasts to myofibroblasts, which can be identified by their de novo synthesis of α-SMA. A human pulmonary fibroblast cell line (WI38-VA13) was tested for induction of α-SMA in a 2D culture using flow cytometry, which allows for the analysis of individual cells in a large cell population with high efficiency. TGF-β1, a potent inducer of fibrosis and

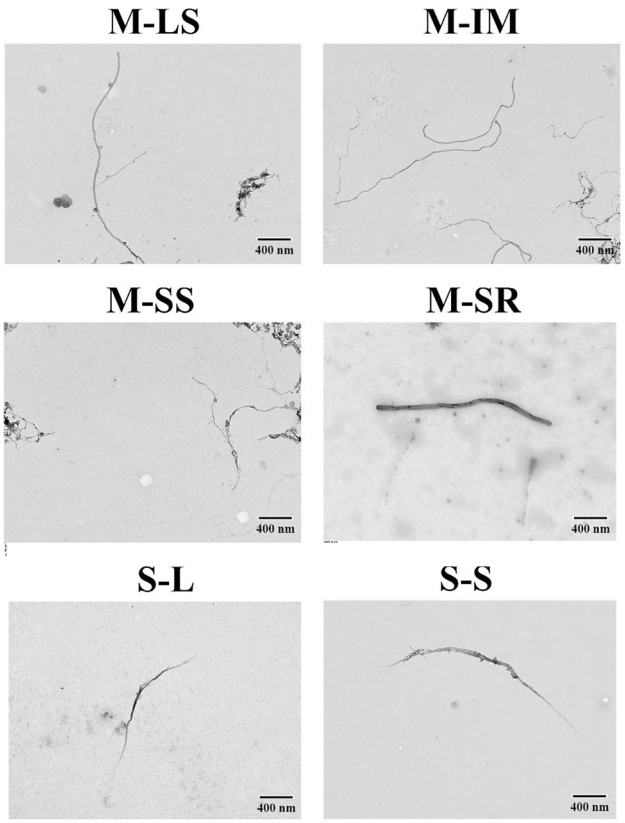

Fig. 1 Transmission electron microscopy of CNTs. TEM was performed on stock solutions of CNTs diluted in double distilled water. Shown are individual fibers and, in some cases, tangles or aggregates that are representative of these samples, especially, M-LS, M-IM, and M-SS. Final magnification of the images is ×10,000. Scale bars are 400 nm. Dimensions of particulate inducers are listed as the following: M-LS has an average diameter of 12 nm, an average length of 10 µm, and a specific surface area of 200 m^2/g; M-IM has an average diameter of 10 nm, an average length of 3–6 µm, and a specific surface area of 280–350 m^2/g; M-SS has an average diameter of 9.5 nm, an average length of 1 µm, and a specific surface area of 300 m^2/g; M-SR has an average diameter of 49 nm, an average length of 3.68 µM, and a specific surface area of 22 m^2/g; S-L has a diameter of 0.7–1.1 nm, a length of 0.3–2.3 µm, and a specific surface area of 700 m^2/g; and S-S has a diameter of 1–2 nm, a length of 0.5-2 mm, and a specific surface area of 480 m^2/g. The MIN-U-SIL 5 silica has 97% of the particles < 5 µm, a median diameter of 1.6 µm, a specific density of 2.65, and silicon dioxide (SiO_2) content of 99.2% and iron oxide (Fe_2O_3) content of 0.035%

α-SMA expression, was used as a positive control (2 ng/mL). Respirable crystalline silica causes silicosis in humans upon inhalation, and is therefore included for comparison with CNTs for their fibrogenic activities. The concentrations used for TGF-β1 and each particulate inducer were first evaluated individually in concentration–response studies, from which a concentration at 1 µg/mL was chosen for all particulate inducers to produce optimal induction.

TGF-β1-treated cells had the highest percentage of cells expressing α-SMA. Figure 2a–i shows representative dot plots for the treatment groups and Fig. 2j presents the average percentage of α-SMA-positive cells. After 24 h of treatment, nearly all TGF-β1-treated cells were positive for α-SMA expression, whereas < 1% of VC cells expressed α-SMA, revealing a high sensitivity and specificity of the assay. An average of 72% of silica-treated cells were positive for α-SMA expression. This result indicates that silica potently induces α-SMA expression, which is consistent with the notion that crystalline silica is a strong inducer of fibrosis in humans and animal models. For each CNT treatment, there was a significant increase in α-SMA-expressing cells compared with VC. For each of the MWCNTs tested, greater than 75% of the cells were positive for α-SMA, higher than that of silica. M-LS and M-SR had the highest percentage of positive cells, at 89 and 85%, respectively. S-L and S-S SWCNTs had 69 and 72% α-SMA-positive cells, comparable to silica treatment, but significantly lower than TGF-β1 or M-LS. Therefore, CNTs directly stimulate robust myofibroblast activation at levels comparable to TGF-β1 and higher than silica in this quantitative in vitro assay by flow cytometry.

CNTs and silica induced localization of α-SMA to stress fibers

Contraction by myofibroblasts is mediated through contractile stress fibers containing newly synthesized α-SMA, which increases the cells' contractile ability. Hence, localized expression of α-SMA to stress fibers and the appearance of thick, contractile stress fibers are two functional markers of myofibroblast transformation. Cells were probed for α-SMA (green) and F-actin (red) in order to determine the localization of α-SMA and changes in cytoskeleton. As expected, VC cells showed no detectable expression of α-SMA, whereas cells treated with TGF-β1 had substantially increased α-SMA staining, as shown in Fig. 3a and quantified in Fig. 3b. Moreover, TGF-β1-treated cells exhibited an increased number of thick, contractile stress fibers (indicated by white arrowheads) compared with VC. Localization of α-SMA to stress fibers can clearly be observed in the merged channel image where yellow marks the overlap between α-SMA and F-actin channels (indicated by cyan arrowheads). Therefore, TGF-β1-treated fibroblasts differentiated into highly contractile myofibroblasts.

All CNTs, as well as silica, increased the expression of α-SMA compared with VC, with M-LS having the highest induction (Fig. 3a, b). M-LS-treated fibroblasts also had an increased number of contractile stress fibers containing α-SMA. Other MWCNTs induced variable amounts of α-SMA expression, appearance of contractile fibers, and localization of α-SMA to stress fibers, which were less in intensity than M-LS, but comparable to silica and higher than SWCNTs. The differences among different CNT

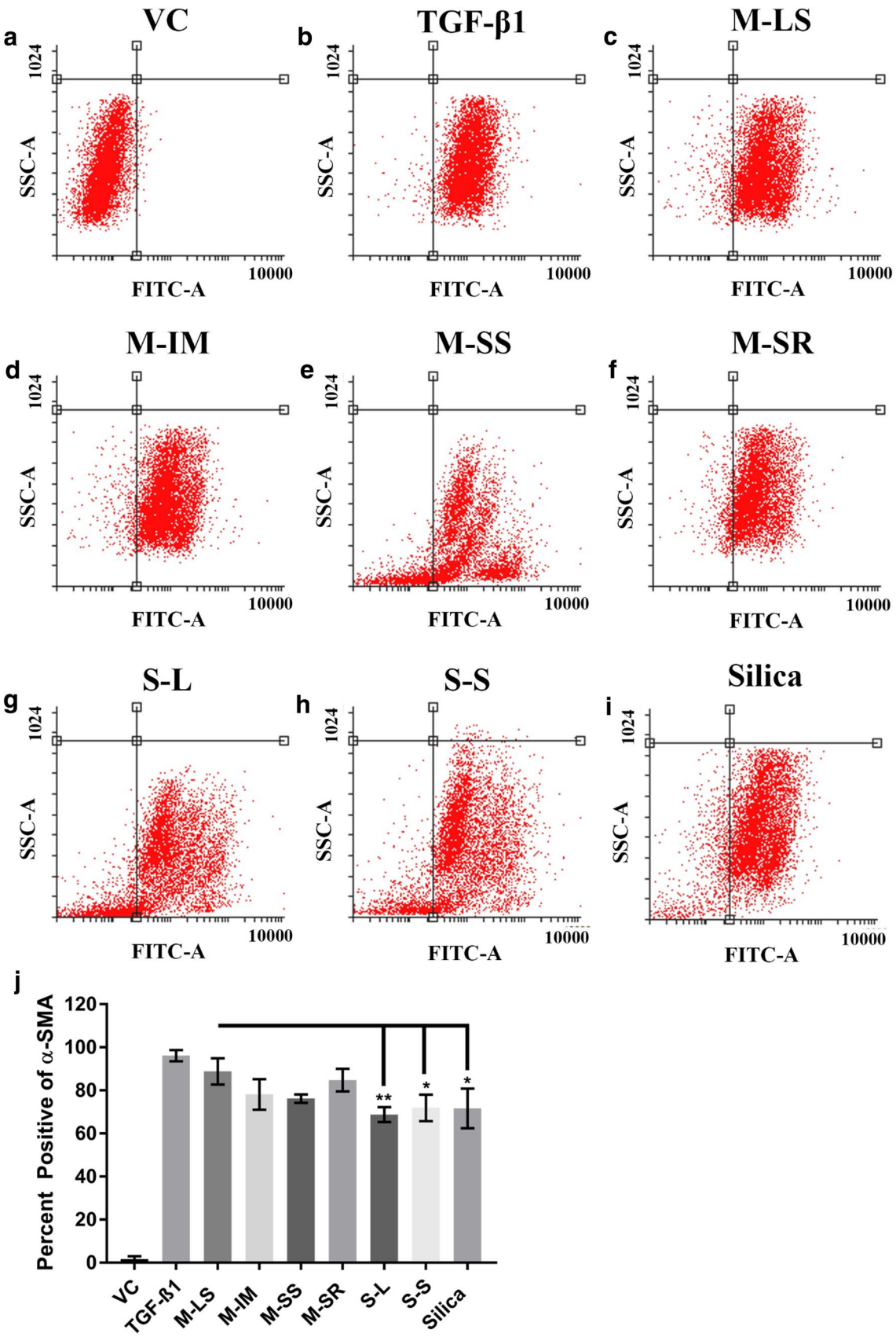
a
VC
b
TGF-β1
c
M-LS
d
M-IM
e
M-SS
f
M-SR
g
S-L
h
S-S
i
Silica
SSC-A
FITC-A
1024
10000
j
Percent Positive of α-SMA
120
100
80
60
40
20
0
VC
TGF-ß1
M-LS
M-IM
M-SS
M-SR
S-L
S-S
Silica
**
*
*

◂**Fig. 2** Flow cytometry measurement of α-SMA expression. **a–i** Representative histograms of α-SMA expression in fibroblasts as measured by flow cytometry are shown. **j** The average percentage of α-SMA-positive cells was calculated for each treatment across three separate experiments. As M-LS had the highest induction among particulate inducers, statistical comparison between M-LS and each other particulate inducer is shown to indicate differential induction of α-SMA. $*p < 0.05$; $**p < 0.01$

treatments are more pronounced and reaches statistical significance as measured by immunofluorescence staining (Fig. 3b). Silica induced α-SMA expression and stress fiber formation at levels comparable to those of M-SS and M-SR. Together, these data indicate that CNTs and silica not only stimulated α-SMA expression, but also induced its incorporation into the stress fibers and increased contractile stress fibers, and these changes in cytoskeletal structure can be distinguished among different nanoparticles.

Induction of α-SMA in 3D culture by CNTs and silica

In traditional 2D systems, cells interact with the inducers only on their surface bathing in the medium and cell–cell interactions are limited to those between adjacent cells through their sides of direct contact, which deviates from in vivo scenarios. On the other hand, fibroblasts cultured in a 3D matrix extend their processes in three dimensions, which effectively increases the cellular surface area and, more importantly, allows cells to receive signals in all directions and from distance, which mimics the cell microenvironment in vivo. Therefore, we set out to establish a 3D culture of myofibroblast differentiation.

A collagen-based gel matrix was used to create a 3D culture in which fibroblasts and inducers were evenly distributed. Expression of α-SMA was measured for myofibroblast differentiation by immunofluorescence imaging (Fig. 4). As expected, VC-treated cells had very little expression of α-SMA with a RFU of merely 0.1. Treatment with TGF-β1 induced a marked increase in α-SMA expression to 28.1 RFU. Cells treated with CNTs also expressed significant amounts of α-SMA. M-LS-treated cells had a relative expression of 27.8 RFU, M-IM 18.5, M-SS 20.1, and M-SR 25.4. Both SWCNTs induced less intense α-SMA expression than MWCNTs. Induction by silica was similar to that by M-SR. Therefore, the 3D collagen construct model used here allows quantification of myofibroblast activation and differentiates among CNTs and silica for their inducing activity.

To visualize cell morphology, and cell–cell and cell–matrix interactions in three dimensions, representative images of collagen constructs stained for α-SMA were used to generate surface projections (Fig. 5). Projections were generated using the F-actin channel to ensure that the entire cell body was captured in the surface projection and individual cells were color-coded according to the intensity of α-SMA staining. The color coding ranges from dark blue, indicating no staining, to red, the most intense staining. Panels on the left are the 3D surface projections as imaged, while panels in the right hand column are the images as seen from the z-axis, which allows the observation of how cells interact with each other in all dimensions. The general morphology of the cells is typical of that seen in fibroblasts in 3D cultures. The cells form processes which often contain focal adhesions and other cell adhesion complexes that enable the cells to "feel", manipulate, and anchor themselves to the surrounding matrix (Doyle and Yamada 2016).

Three features of the cells are readily seen from these images. First, these images generate a visual representation of the quantitative data presented in Fig. 4 for α-SMA expression. VC cells are color-coded as dark blue, indicating no α-SMA staining. Cells treated with either TGF-β1, M-LS, M-SS, or M-SR had significant numbers of cells color-coded red, with nearly no cells at the lower end of the spectrum, indicating high amounts of α-SMA staining. Cells treated with M-IM are in the light blue to orange range of the spectrum, while SWCNT-treated cells are mainly in the blue to green range of the spectrum with a small fraction of cells in red, indicating an overall low level of α-SMA staining. Cells treated with silica exhibited red, yellow, and green colors, at levels comparable to those in M-LS, M-IM, or M-SR-treated cells. Second, the panels on the right, showing the *z*-axis view, reveal that cells in different focal planes of the collagen construct are interacting with each other, with processes extended throughout the depth of the image, as expected from a 3D culture. Third, cells with similar levels of α-SMA staining tend to cluster together, as is especially evident in the red and green clusters of cells. This could indicate local release of TGF-β1 or other signaling factors from cells directly interacting with CNTs, or a local change to the collagen matrix which affects nearby cells, resulting in a feed forward loop of myofibroblast differentiation among nearby cells.

CNTs and silica induced remodeling of collagen matrix

To examine myofibroblast–matrix interactions and their modulation by CNTs in 3D culture, the collagen matrix was visualized using Masson's trichrome staining and analyzed for fibrotic-like properties. Representative images are shown in Fig. 6a. The amount of collagen staining in the samples, which reflects both elevated collagen deposition and increased collagen bundling, was quantified and is presented as the average staining intensity (Fig. 6b). Cells treated with either TGF-β1 or CNTs showed markedly increased collagen staining surrounding the cells. Samples treated with M-LS had the highest amount of collagen staining, followed by samples treated with M-SR, then by samples treated with

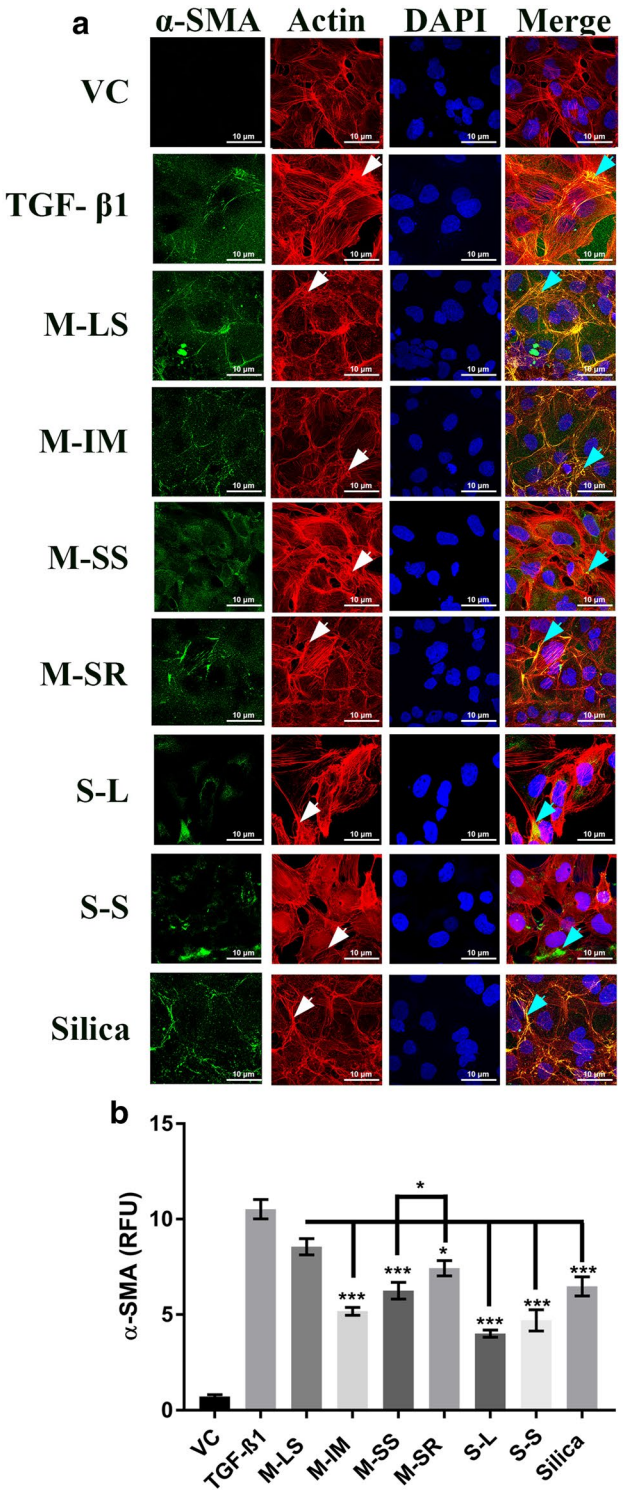

Fig. 3 α-SMA expression and localization with stress fibers. Fibroblasts were treated as indicated for 24 h before being stained for α-SMA (green channel), F-actin (red channel), and DAPI (blue channel). **a** Representative images are shown. White arrowheads on the F-actin channel indicate areas containing contractile stress fibers and cyan arrows on the merged images indicate α-SMA localized to stress fibers. **b** α-SMA staining is presented in RFU as means ± SD from three separate experiments. Statistical comparison between M-LS and each other particulate inducer and between M-SS and M-SR is shown. $*p < 0.05$; $***p < 0.001$

silica, TGF-β1, M-IM, and M-SS; and lastly by samples treated with S-L and S-S. Notably, areas with increased collagen staining corresponded with the presence of CNT fibers and aggregates nearby (indicated by arrowheads).

The relative alignment of collagen fibers in the area immediately surrounding the cells was determined using the OrientationJ plugin for ImageJ, where a higher coherence coefficient corresponds to a higher level of collagen alignment (Fig. 6c). All treatment groups showed an increase in collagen fiber alignment compared to VC control. Constructs treated with M-LS had the highest coherence with a coherence coefficient of 0.16 ± 0.013, which is significantly higher than those of constructs treated with any of the other CNTs. These results indicate that CNTs and silica induce fibroblasts to alter the surrounding collagen matrix and this effect varies among CNTs with different physicochemical properties, with M-LS producing the highest effect on collagen realignment.

Samples treated with CNTs had an increase in the number of cell clusters, which appear analogous to early stage fibrotic foci seen in lung samples from CNT-exposed animals. For the purpose of this study, cell clusters were defined as 3 or more cells that shared an extended and visibly altered collagen matrix, as can be clearly distinguished in the 100× magnification panels of CNT-treated samples in Fig. 6a. Quantification of the cell clusters is expressed as the number of cell clusters per mm^2 (Fig. 6d), as well as the cell cluster area, i.e., the percentage of the cluster area in the total sample area (Fig. 6e). VC control samples had only minimal cell clusters. Similar to collagen staining and collagen coherence, samples treated with TGF-β1 or particulate inducers had significantly increased cell cluster numbers and cell cluster area, with M-LS producing the highest effects, followed by M-SR, then TGF-β1, M-IM, M-SS, and silica, and lastly S-L and S-S. These data are qualitatively in line with the results for collagen staining and fiber alignment. Therefore, CNTs induced cells to alter the amount and structure of their surrounding collagen matrix and promoted the formation of cell clusters increasing both their number and size, a phenomenon analogous to the fibrotic focus formation observed in vivo.

Cell proliferation was investigated as a mechanism of cell cluster formation. Constructs were stained for Ki67 expression using immunohistochemistry and counterstained with Masson's trichrome (Fig. 7a, quantified in Fig. 7b). Control cells had a relatively low rate of Ki67 expression (21.7%). Treatment with M-LS induced expression in the greatest number of cells, with 63% of cells expressing Ki67. Consistent with collagen fiber alignment and cell cluster analysis, M-LS-induced Ki67 expression was only slightly higher than M-SR treatment (58%), while M-IM treatment induced the lowest level of expression among MWCNT samples at 48%. Finally, SWCNTs

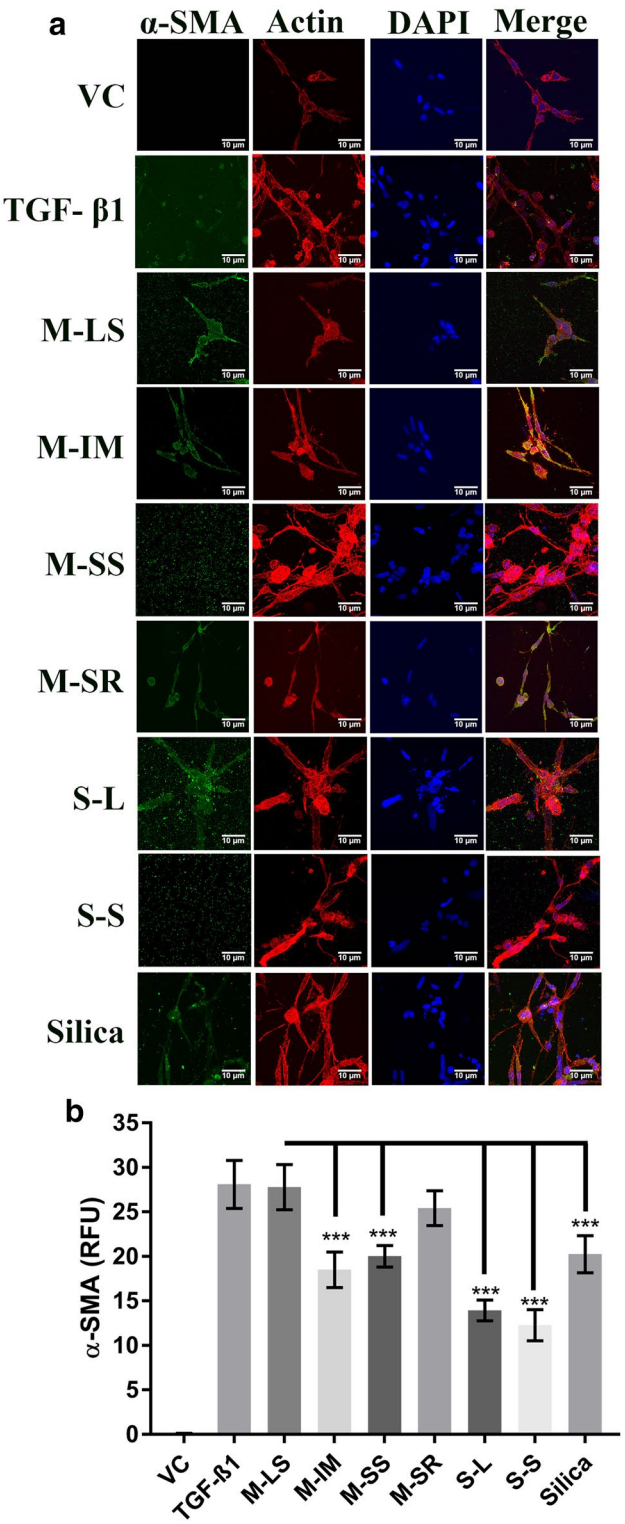

Fig. 4 CNT induced SMA expression and morphology of fibroblasts in 3D culture. Cells were seeded at a density of 1×10^5 cells/mL in 1 mg/mL Type I collagen. Particulate inducers (1 µg/mL) and TGF-β1 (2 ng/mL) were also included in the collagen solution before being poured in a 24 well plate. After collagen polymerization, gels were freed from the edges of the plate and allowed to incubate for 48 h. Constructs were then fixed, polymerized, and stained for α-SMA (green channel), F-actin (red channel), and DAPI before being mounted in a photobleaching resistant mounting media with DAPI. **a** Representative images for each channel and each treatment are shown with merged images on right. **b** The relative intensity of α-SMA staining (RFU) was quantified using Imaris software. Data is presented as mean ± SD from three separate experiments. All treatments induced a significant increase in α-SMA expression compared with VC. As M-LS had the highest induction among particulate inducers, statistical comparison between M-LS and each other particulate inducer is shown to indicate differential induction of α-SMA among particulate inducers. ***$p < 0.001$

induced a relatively modest level of Ki67 expression (29.7% and 32.7%). Silica increased Ki67 expression to a level similar to that by M-SR. Therefore, CNTs and silica increased cell proliferation, which in part contributes to cell cluster formation.

CNTs stimulated contraction of collagen gels by myofibroblasts

A gel contraction model where cells are allowed to freely contract the collagen matrix was used to examine CNT's effect on matrix contraction, which is measured as the change in diameter of the collagen gel and is expressed as percent contraction. VC-treated cells had a baseline contraction of 20.5%, attributable to an intrinsic fibroblast contraction (Fig. 8). The optimal concentration for TGF-β1 was determined to be 2 ng/mL, which induced contraction to 40.2%, more than double that of VC (Fig. 8). For each of the CNTs tested, a concentration range of 0.25–10 µg/mL was examined and the highest gel contraction for each CNT was found to occur at the concentration of 1 µg/mL (Fig. 8, data not shown). Therefore, 1 µg/mL of particulates was used to examine gel contraction.

M-LS induced 45.6% contraction, which is the highest contraction among all treatments and is significantly higher than cells treated with M-IM, S-L, S-S, or silica, or is higher than cells treated with M-SS and M-SR but without statistical significance (Fig. 8). SWCNTs produced significantly lower gel contraction than MWCNTs and S-S were only able to contract the gels by 24.7%, which is similar to VC. These results are qualitatively similar to the α-SMA induction data in 3D collagen constructs. Therefore, myofibroblasts induced by CNTs and silica demonstrate increased capacity to contract their matrix in this 3D collagen model, which reflects the ability of CNTs and silica to stimulate fibrotic contraction in vitro.

Discussion

The potential of CNTs to cause fibrosis in lungs has been a major concern in occupational safety and health as well as consumer and environmental protection (Donaldson et al.

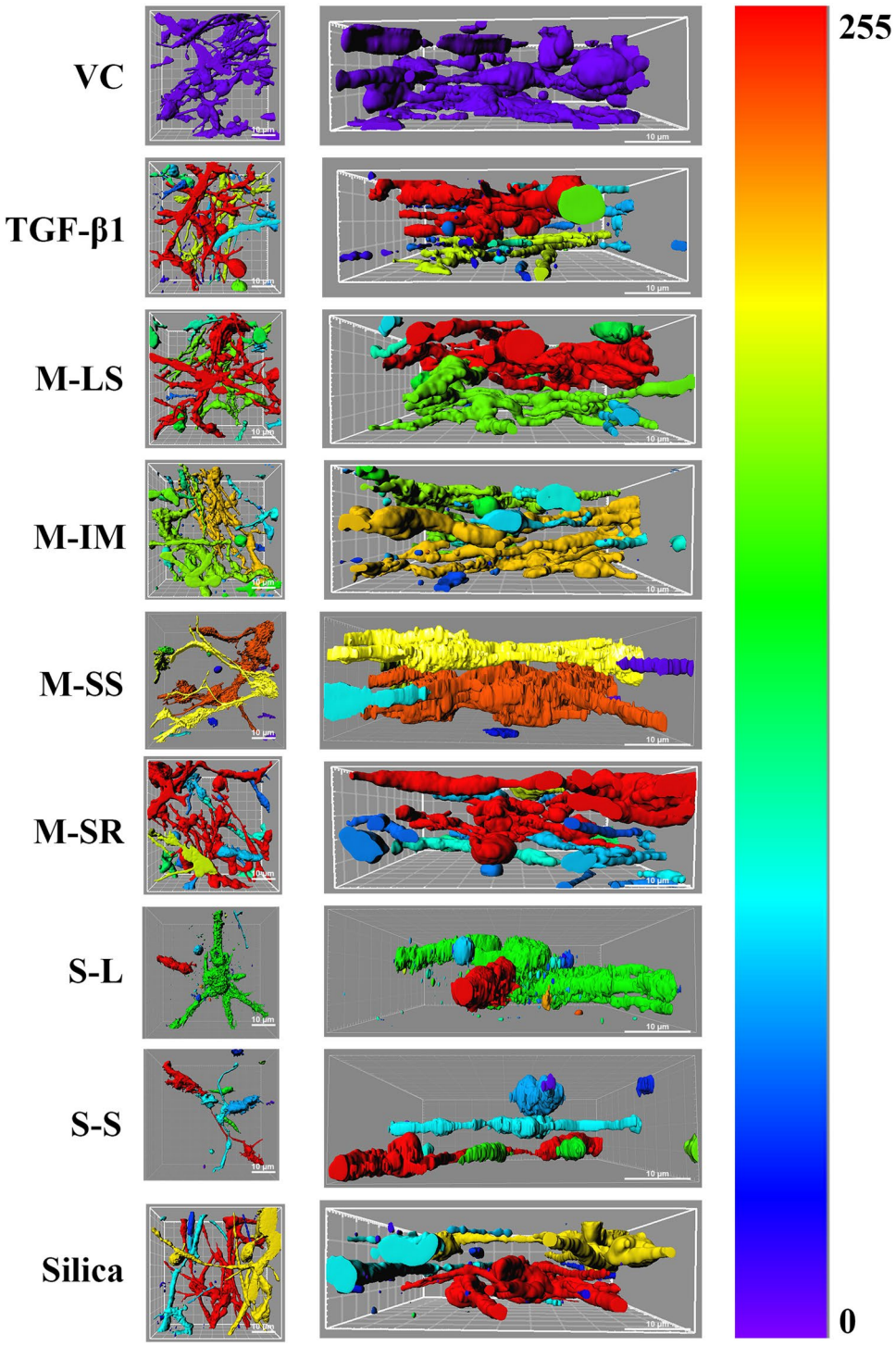

Fig. 5 α-SMA expression, morphology, and projections of fibroblasts in 3D culture. Cells were seeded in 1 mg/mL Type I collagen including particulate inducers or TGF-β1 before being poured in a 24-well plate. After collagen polymerization, gels were freed from the edges of the plate and allowed to incubate for 48 h. Constructs were then fixed, polymerized, and stained for α-SMA and F-actin before being mounted in a mounting media with DAPI. Z-stacks were acquired using confocal microscopy and images were analyzed using Imaris software. Surface projections were generated using the F-actin channels and surfaces were color-coded according to their relative α-SMA intensity. Images in the left column are the *x*–*y* plane projection, while images in the right columns are the *x*–*z* plane projection

2006; Dong and Ma 2015). However, investigating the fibrogenic potential of CNTs can be a time- and resource-consuming process due to the lack of replicable, verified in vitro models. In vitro systems generally have the advantage of being efficient, inexpensive, and adaptive for large-scale screening in comparison with animal studies. But the in vitro models for fibrosis would need to account for a large role of the ECM in the fibrotic process and offer a way to measure the activation of myofibroblasts by both traditional biomarkers and functional changes, attributes that most conventional in vitro systems do not possess. In addition, any in vitro model must be sensitive enough to detect differences in fibrogenic potential among CNTs. From this prospective, there has been a rapidly growing trend in using 3D cultures

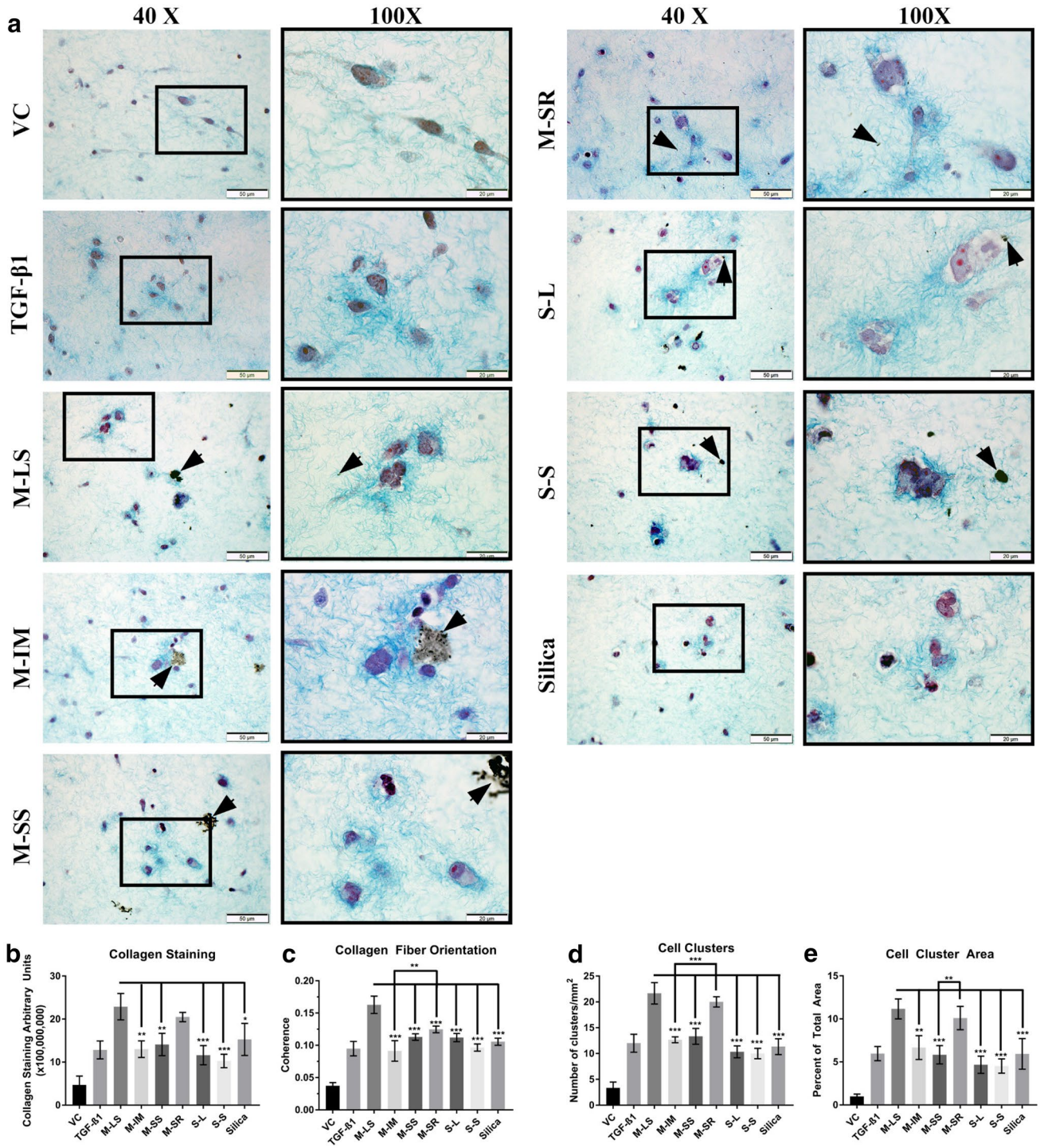

Fig. 6 Collagen matrix remodeling induced by CNTs. Collagen gel constructs were prepared as described for Fig. 3. The constructs were stained using Masson's trichrome to visualize the collagen matrix. Shown are representative images at both ×40 and ×100 magnifications (**a**), quantification of collagen staining (**b**), collagen fiber orientation (**c**), number of cell clusters (**d**), and cell cluster area (**e**), for each treatment. Data were collected in triplicate and is presented as mean ± SD. Statistical analysis was performed and shown as described for Fig. 1. $*p < 0.05$; $**p < 0.01$; $***p < 0.001$

for biological screening and mechanistic analysis because of several apparent advantages to 3D assays. For instance, cells in 3D cultures form attachments to each other and to their surroundings in all dimensions (Baker and Chen 2012; Pampaloni et al. 2007; Ravi et al. 2015). 3D models also allow cells to interact with treatment agents across the entire cell.

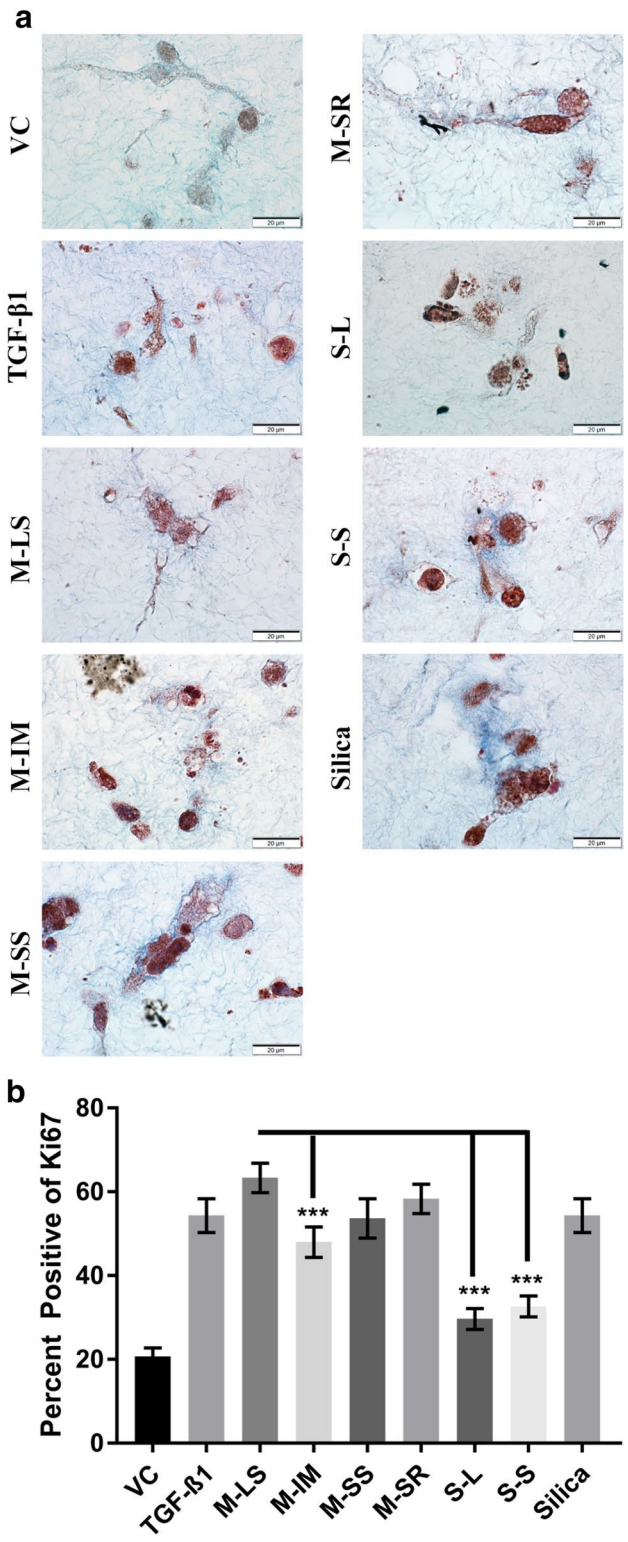

Fig. 7 Ki67 Expression Induced by CNTs. Collagen gel constructs were prepared as described for Fig. 3. Cells were stained for Ki67 expression and the collagen matrix was visualized using a modified Masson's Trichome staining. Shown are representative ×100 magnification images (**a**). Image J was used to quantify the percentage of cells expressing Ki67 (**b**). Data were collected in triplicate and is presented as mean ± SD. Statistical analysis was performed and shown as described for Fig. 1. $*p < 0.05$; $**p < 0.01$; $***p < 0.001$

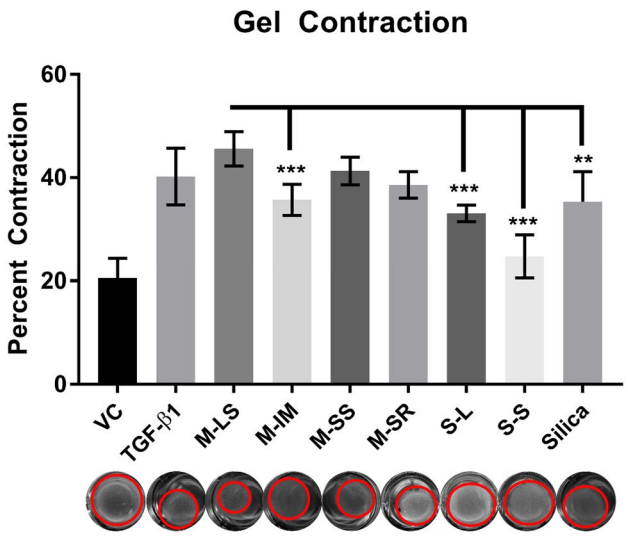

Fig. 8 Collagen gel contraction assay. Collagen gel constructs were poured as described for Fig. 3 and fibroblasts were allowed to contract the collagen gel for 48 h. Data were collected in triplicate across three separate experiments and presented as mean ± SD. Representative images of the contracted gels are shown at the bottom with red circles outlining the boundaries of contracted gels. Statistical analysis was performed and shown as described for Fig. 1. $**p < 0.01$; $***p < 0.001$

Therefore, 3D cultures mimic the in vivo cellular environment for cell–cell, cell–matrix, and cell–inducer interactions better than many traditional 2D cultures. This feature of 3D cultures is especially important for studying diseases like fibrosis that has a large ECM component (Blaauboer et al. 2014; Van De Water et al. 2013).

In this study, we identified and validated a collagen-based 3D model as a potential in vitro model of pulmonary fibrosis. In this 3D system, induced differentiation of human pulmonary fibroblasts to myofibroblasts, as well as the functions of the myofibroblasts and their interaction with their matrix and the particulate inducers, can be analyzed and visualized at cellular and molecular levels. To achieve this goal, human pulmonary fibroblasts were treated with 6 CNTs of varying physicochemical properties or silica, and their fibrogenic potentials were measured across several assays, including traditional 2D culture-based assays and a new, collagen-based 3D system, in comparison with vehicle control and TGF-β1, a known inducer of fibrosis with high potency.

Differentiation of fibroblasts into myofibroblasts is a critical step toward fibrosis development and expression of α-SMA is a commonly used marker of myofibroblast formation (Dong and Ma 2016b). We used two different approaches to measure CNT's ability to induce α-SMA expression in fibroblasts, i.e., flow cytometry, which quantifies the inductive response in a large cell population, and immunofluorescence staining, which images and quantifies α-SMA localization and expression in single and group cells.

All CNTs tested induced expression of α-SMA in a significant percentage of the cell population. However, MWCNTs induced expression to a greater degree than SWCNTs. Cells treated with CNTs expressed high levels of α-SMA that localized to cytoskeleton-associated stress fibers, which indicates myofibroblast activation. In these studies, quantification of α-SMA reveals differential induction by TGF-β1, each MWCNTs and SWCNTs, and silica compared with vehicle control, whereas imaging of α-SMA expression uncovers unique shapes and behaviors of myofibroblasts in 3D cultures that mimic in vivo systems, such as the formation of contractile stress fibers and clustering of activated myofibroblasts.

Changes in the organization of the collagen matrix are integral components of wound healing and fibrosis, including contributing to myofibroblast differentiation and activation (Tschumperlin et al. 2018; Xue and Jackson 2015). Certain changes to collagen fiber orientation, specifically the degree of fiber alignment, are associated with a more stiff matrix (Xu et al. 2011). We visualized and measured these changes to the collagen matrix using Masson's trichrome staining. The intensity of collagen staining was significantly increased in samples treated with CNTs and silica, indicating increased synthesis and secretion of collagen from activated myofibroblasts. Moreover, cells treated with CNTs and silica organized their surrounding matrix to a significantly higher degree indicating induced fiber alignment and stiffness.

Increased stiffness of the matrix provides a ready scaffold for potential cell migration through a process called durotaxis (Asano et al. 2017; Baker and Chen 2012). This phenomenon may play a role in the formation of the cell clusters observed in this study, which mimics the formation of fibrotic foci in vivo. In this scenario, once one cell is activated to a contractile myofibroblast and alters the surrounding matrix, the resulting change in matrix tension may draw nearby cells to migrate toward the initially activated cell. Alternatively, proliferation of activated cells may be responsible for the formation of cell clusters (Chilosi et al. 2006). Increased tension on the ECM releases latent TGF-β1 from the matrix (Marinkovic et al. 2012), providing an additional mechanism for a feed forward loop between activated fibroblasts and the diseased matrix. Indeed, we found that CNT treatment significantly increased cell proliferation within cell clusters. As matrix contraction is a major process in fibrosis to lead to scarring, the contractile ability of cells treated with various CNTs was determined using a gel contraction assay, which allows the direct measurement of the contractile capabilities of a population of cells. Consistent with α-SMA expression, MWCNTs induced gel contraction to a greater degree than SWCNTs, with M-LS producing the greatest effect on gel contraction. Together, these particulate-induced changes in matrix remodeling, formation of cell clusters, and matrix contraction provide new insights into the nature of matrix–fibroblast interactions, an important aspect of studying fibrotic responses induced by CNTs.

Previous studies have postulated that the aspect ratio of CNTs plays a role in CNT toxicity including lung fibrosis (Hamilton et al. 2013; Liu et al. 2016; Murphy et al. 2011; Sanchez et al. 2011; Sweeney et al. 2015), i.e., CNTs with a high aspect ratio would produce more apparent toxic phenotypes than CNTs with lower aspect ratios. Our results agree with this prediction on M-LS, M-IM, and M-SS, but deviates on the CNTs with a very low aspect ratio, i.e., M-SR, which is short, thick, and rigid. Notably, these previous studies were performed in animals (Hamilton et al. 2013; Murphy et al. 2011), or on cultured macrophages (Sanchez et al. 2011; Sweeney et al. 2015) or endothelial cells (Liu et al. 2016), and with different CNTs, which may contribute to differences in the results from different studies. Alternatively, Hamilton et al. (2013) observed that there was an increase in toxicity as either the diameter or the length of the MWCNT increased. The two MWCNTs with the highest induction of α-SMA expression in this study were those with the longest length, M-LS, and highest diameter, M-SR, which is consistent with this notion. Therefore, length, diameter, and rigidity are consistently found to be among the most important physical properties in determining the relative fibrogenicity of CNT fibers. Similar conclusions have been made by others with respect to fibrosis in mouse lungs and tumorigenesis in mouse lungs and pleural space (Bussy et al. 2013; Duke and Bonner 2018; Duke et al. 2018; Nagai et al. 2011; Nagai and Toyokuni 2012).

Interestingly, though M-SR induced high expression of α-SMA and increased collagen staining and alignment, this did not correlate to a significant increase in matrix contraction. These findings suggest that M-LS and M-SR stimulate myofibroblast differentiation and activation via overlapping but distinguishable mechanisms, which deserves further investigation. Of the CNTs investigated here, M-SR is the most studied in vivo, where it has been shown to potently induce pulmonary fibrosis in rodent models. Notably, in these systems, M-SR dosing induced significant immune responses, activating leukocytes to produce an array of cytokines, chemokines, and growth factors (Dong and Ma 2016a, 2018a, b). Further studies are needed to define and dissect phenotypic and mechanistic differences between M-LS and M-SR MWCNTs. Silica induced fibrotic changes that are comparable to those by M-SS and M-SR for many of the assays, which is consistent with their strong fibrogenic activity in the lungs (Dong et al. 2015, 2016).

The results of this study indicate that the 3D collagen-based model allows for the investigation of the ability of CNTs to induce fibrosis in a defined and controlled environment. This system is effective and versatile, allowing for the detailed examination of multi-aspects of cells and the collagen matrix in relation to fibrosis. In this study, we

demonstrated that the 3D collagen constructs can be fixed and stained for α-SMA for myofibroblast differentiation and functioning, whereas collagen matrix remodeling, cell clustering, and contraction within the matrix can be visualized and quantified by tissue staining. This system can also be adapted for other types of fibrosis investigations. For instance, expression of particular matrix proteins and regulators can be examined in this 3D culture for the identification of biomarkers of exposure and pathogenesis. Macrophages and epithelial cells are known to contribute to fibrotic development and investigating how these cells contribute to fibroblast contractile ability in the 3D collagen model with co-cultures of fibroblasts and the cells of interest would reveal new aspects of how these cells modulate fibrogenesis and fibrotic progression caused by CNTs, silica, and other particulate inducers in future studies.

In conclusion, the rapidly increased production and use of many types of CNTs, along with the findings from animal studies revealing fibrogenic potentials of some CNTs, call for effective and timely toxicological evaluation of CNTs, especially on their fibrogenic activities. Because of the large numbers of CNTs available on the market and numerous ways these nanomaterials can be modified in ways that may affect toxicity, in vivo animal testing is far from being capable of meeting this vastly increased demand, both economically and in terms of efficiency. Therefore, in vitro models that can be used to quickly and efficiently investigate the relative toxicity of CNTs would be invaluable. In this regard, induction of α-SMA expression in cultured cells is shown to be a quantitative and robust marker of myofibroblast differentiation, whereas the collagen-based 3D model is demonstrated to effectively evaluate the fibrogenic potentials of CNTs and particulate inducers by measuring the function and behaviors of activated myofibroblasts, as well as the production, remodeling, and contraction of the matrix, in vitro. Modification of these parameters by CNTs and their mode of action are dependent upon their physical dimensions, with the length, diameter, and rigidity as the most affecting factors.

Acknowledgements The authors thank A. Winn for assistance on flow cytometry measurement of α-SMA, S. Friend on TEM imaging of CNTs, D.L. Richardson and L.A. Battelli on histological processing and staining, Dr. D.W. Porter for providing M-SR (XNRI MWNT-7, Mitsui) and silica (Min-U-Sil 5), and M.G. Wolfarth on CNT preparation.

Funding This work was funded to Q.M. by the Health Effects Laboratory Division and the Nanotechnology Research Center at National Institute for Occupational Safety and Health, Centers for Disease Control and Prevention, USA. No. 8939050W.

Compliance with ethical standards

Conflict of interest The authors declare there are no competing financial interests. The findings and conclusions in this report are those of the authors and do not necessarily represent the official position of the National Institute for Occupational Safety and Health, Centers for Disease Control and Prevention.

References

Asano S, Ito S, Takahashi K et al (2017) Matrix stiffness regulates migration of human lung fibroblasts. Physiol Rep 5(9):e13281. https://doi.org/10.14814/phy2.13281

Baker BM, Chen CS (2012) Deconstructing the third dimension: how 3D culture microenvironments alter cellular cues. J Cell Sci 125(Pt 13):3015–3024. https://doi.org/10.1242/jcs.079509

Birch ME, Ruda-Eberenz TA, Chai M, Andrews R, Hatfield RL (2013) Properties that influence the specific surface areas of carbon nanotubes and nanofibers. Ann Occup Hyg 57(9):1148–1166. https://doi.org/10.1093/annhyg/met042

Blaauboer ME, Boeijen FR, Emson CL et al (2014) Extracellular matrix proteins: a positive feedback loop in lung fibrosis? Matrix Biol 34:170–178. https://doi.org/10.1016/j.matbio.2013.11.002

Bussy C, Ali-Boucetta H, Kostarelos K (2013) Safety considerations for graphene: lessons learnt from carbon nanotubes. Acc Chem Res 46(3):692–701. https://doi.org/10.1021/ar300199e

Chilosi M, Zamo A, Doglioni C et al (2006) Migratory marker expression in fibroblast foci of idiopathic pulmonary fibrosis. Respir Res 7:95. https://doi.org/10.1186/1465-9921-7-95

Donaldson K, Aitken R, Tran L et al (2006) Carbon nanotubes: a review of their properties in relation to pulmonary toxicology and workplace safety. Toxicol Sci 92(1):5–22. https://doi.org/10.1093/toxsci/kfj130

Dong J, Ma Q (2015) Advances in mechanisms and signaling pathways of carbon nanotube toxicity. Nanotoxicology 9(5):658–676. https://doi.org/10.3109/17435390.2015.1009187

Dong J, Ma Q (2016a) In vivo activation of a T helper 2-driven innate immune response in lung fibrosis induced by multi-walled carbon nanotubes. Arch Toxicol 90(9):2231–2248. https://doi.org/10.1007/s00204-016-1711-1

Dong J, Ma Q (2016b) Myofibroblasts and lung fibrosis induced by carbon nanotube exposure. Part Fibre Toxicol 13(1):60. https://doi.org/10.1186/s12989-016-0172-2

Dong J, Ma Q (2016c) Suppression of basal and carbon nanotube-induced oxidative stress, inflammation and fibrosis in mouse lungs by Nrf2. Nanotoxicology 10(6):699–709. https://doi.org/10.3109/17435390.2015.1110758

Dong J, Ma Q (2017a) Osteopontin enhances multi-walled carbon nanotube-triggered lung fibrosis by promoting TGF-beta1 activation and myofibroblast differentiation. Part Fibre Toxicol 14(1):18. https://doi.org/10.1186/s12989-017-0198-0

Dong J, Ma Q (2017b) TIMP1 promotes multi-walled carbon nanotube-induced lung fibrosis by stimulating fibroblast activation and proliferation. Nanotoxicology 11(1):41–51. https://doi.org/10.1080/17435390.2016.1262919

Dong J, Ma Q (2018a) Macrophage polarization and activation at the interface of multi-walled carbon nanotube-induced pulmonary inflammation and fibrosis. Nanotoxicol. https://doi.org/10.1080/17435390.2018.1425501 **(in press)**

Dong J, Ma Q (2018b) Type 2 Immune Mechanisms in Carbon Nanotube-Induced Lung Fibrosis. Front Immunol 9:1120. https://doi.org/10.3389/fimmu.2018.01120

Dong J, Porter DW, Batteli LA, Wolfarth MG, Richardson DL, Ma Q (2015) Pathologic and molecular profiling of rapid-onset fibrosis and inflammation induced by multi-walled carbon nanotubes. Arch Toxicol 89(4):621–633. https://doi.org/10.1007/s00204-014-1428-y

Dong J, Yu X, Porter DW, Battelli LA, Kashon ML, Ma Q (2016) Common and distinct mechanisms of induced pulmonary fibrosis by particulate and soluble chemical fibrogenic agents. Arch Toxicol 90(2):385–402. https://doi.org/10.1007/s00204-015-1589-3

Doyle AD, Yamada KM (2016) Mechanosensing via cell–matrix adhesions in 3D microenvironments. Exp Cell Res 343(1):60–66. https://doi.org/10.1016/j.yexcr.2015.10.033

Duffield JS, Lupher M, Thannickal VJ, Wynn TA (2013) Host responses in tissue repair and fibrosis. Annu Rev Pathol 8:241–276. https://doi.org/10.1146/annurev-pathol-020712-163930

Duke KS, Bonner JC (2018) Mechanisms of carbon nanotube-induced pulmonary fibrosis: a physicochemical characteristic perspective. Wiley Interdiscip Rev Nanomed Nanobiotechnol 10(3):e1498. https://doi.org/10.1002/wnan.1498

Duke KS, Taylor-Just AJ, Ihrie MD et al (2017) STAT1-dependent and -independent pulmonary allergic and fibrogenic responses in mice after exposure to tangled versus rod-like multi-walled carbon nanotubes. Part Fibre Toxicol 14(1):26. https://doi.org/10.1186/s12989-017-0207-3

Duke KS, Taylor AJ, Ihrie MD, Shipkowski KA, Needham EC, Bonner JC (2018) Signal transducer and activator of transcription 1 regulates multiwalled carbon nanotube-induced pulmonary fibrosis in mice via suppression of transforming growth factor-beta1 production and signaling. Ann Am Thorac Soc 15(Supplement_2):S129–S130. https://doi.org/10.1513/AnnalsATS.201707-588MG

Hamilton RF Jr, Wu Z, Mitra S, Shaw PK, Holian A (2013) Effect of MWCNT size, carboxylation, and purification on in vitro and in vivo toxicity, inflammation and lung pathology. Part Fibre Toxicol 10(1):57. https://doi.org/10.1186/1743-8977-10-57

Liu F, Mih JD, Shea BS et al (2010) Feedback amplification of fibrosis through matrix stiffening and COX-2 suppression. J Cell Biol 190(4):693–706. https://doi.org/10.1083/jcb.201004082

Liu X, Wu F, Tian Y et al (2016) Size dependent cellular uptake of rod-like bionanoparticles with different aspect ratios. Sci Rep 6:24567. https://doi.org/10.1038/srep24567

Lygoe KA, Norman JT, Marshall JF, Lewis MP (2004) AlphaV integrins play an important role in myofibroblast differentiation. Wound Repair Regen 12(4):461–470. https://doi.org/10.1111/j.1067-1927.2004.12402.x

MacDonald RA, Laurenzi BF, Viswanathan G, Ajayan PM, Stegemann JP (2005) Collagen-carbon nanotube composite materials as scaffolds in tissue engineering. J Biomed Mater Res A 74(3):489–496. https://doi.org/10.1002/jbm.a.30386

Marinkovic A, Mih JD, Park JA, Liu F, Tschumperlin DJ (2012) Improved throughput traction microscopy reveals pivotal role for matrix stiffness in fibroblast contractility and TGF-beta responsiveness. Am J Physiol Lung Cell Mol Physiol 303(3):L169–L180. https://doi.org/10.1152/ajplung.00108.2012

Mitchell LA, Gao J, Wal RV, Gigliotti A, Burchiel SW, McDonald JD (2007) Pulmonary and systemic immune response to inhaled multiwalled carbon nanotubes. Toxicol Sci 100(1):203–214. https://doi.org/10.1093/toxsci/kfm196

Murphy FA, Poland CA, Duffin R et al (2011) Length-dependent retention of carbon nanotubes in the pleural space of mice initiates sustained inflammation and progressive fibrosis on the parietal pleura. Am J Pathol 178(6):2587–2600. https://doi.org/10.1016/j.ajpath.2011.02.040

Nagai H, Toyokuni S (2012) Differences and similarities between carbon nanotubes and asbestos fibers during mesothelial carcinogenesis: shedding light on fiber entry mechanism. Cancer Sci 103(8):1378–1390. https://doi.org/10.1111/j.1349-7006.2012.02326.x

Nagai H, Okazaki Y, Chew SH et al (2011) Diameter and rigidity of multiwalled carbon nanotubes are critical factors in mesothelial injury and carcinogenesis. Proc Natl Acad Sci USA 108(49):E1330–E1338. https://doi.org/10.1073/pnas.1110013108

NSF (National Science Foundation) (2011) Nanotechnology research directions for societal needs in 2020: retrospective and outlook summary. In: Roco M, Mirkin C, Hersan M (eds) Science policy reports. Springer, New York

Pampaloni F, Reynaud EG, Stelzer EH (2007) The third dimension bridges the gap between cell culture and live tissue. Nat Rev Mol Cell Biol 8(10):839–845. https://doi.org/10.1038/nrm2236

Porter DW, Hubbs AF, Mercer RR et al (2010) Mouse pulmonary dose- and time course-responses induced by exposure to multi-walled carbon nanotubes. Toxicology 269(2–3):136–147. https://doi.org/10.1016/j.tox.2009.10.017

Puspoki Z, Storath M, Sage D, Unser M (2016) Transforms and operators for directional bioimage analysis: a survey. Adv Anat Embryol Cell Biol 219:69–93. https://doi.org/10.1007/978-3-319-28549-8_3

Ravi M, Paramesh V, Kaviya SR, Anuradha E, Solomon FD (2015) 3D cell culture systems: advantages and applications. J Cell Physiol 230(1):16–26. https://doi.org/10.1002/jcp.24683

Rezakhaniha R, Agianniotis A, Schrauwen JT et al (2012) Experimental investigation of collagen waviness and orientation in the arterial adventitia using confocal laser scanning microscopy. Biomech Model Mechanobiol 11(3–4):461–473. https://doi.org/10.1007/s10237-011-0325-z

Sanchez VC, Weston P, Yan A, Hurt RH, Kane AB (2011) A 3-dimensional in vitro model of epithelioid granulomas induced by high aspect ratio nanomaterials. Part Fibre Toxicol 8:17. https://doi.org/10.1186/1743-8977-8-17

Sweeney S, Grandolfo D, Ruenraroengsak P, Tetley TD (2015) Functional consequences for primary human alveolar macrophages following treatment with long, but not short, multiwalled carbon nanotubes. Int J Nanomed 10:3115–3129. https://doi.org/10.2147/IJN.S77867

Teran FDE (2016) A new approach towards understanding the ion transfer dynamics in nanostructured carbon-based thin films for energy storage applications. Universite Pierre et Marie Curie, Paris

Tschumperlin DJ, Ligresti G, Hilscher MB, Shah VH (2018) Mechanosensing and fibrosis. J Clin Invest 128(1):74–84. https://doi.org/10.1172/JCI93561

Van De Water L, Varney S, Tomasek JJ (2013) mechanoregulation of the myofibroblast in wound contraction, scarring, and fibrosis: opportunities for new therapeutic intervention. Adv Wound Care (New Rochelle) 2(4):122–141. https://doi.org/10.1089/wound.2012.0393

Xu B, Chow MJ, Zhang Y (2011) Experimental and modeling study of collagen scaffolds with the effects of crosslinking and fiber alignment. Int J Biomater 2011:172389. https://doi.org/10.1155/2011/172389

Xue M, Jackson CJ (2015) Extracellular matrix reorganization during wound healing and its impact on abnormal scarring. Adv Wound Care (New Rochelle) 4(3):119–136. https://doi.org/10.1089/wound.2013.0485